ARMY RESEARCH LABORATORY

Heterogeneous Architectures Incorporating Nitride Semiconductors for Enhanced Functionality of Optoelectronic Devices (FY11)

by Anand V. Sampath, Meredith L. Reed, Michael Gerhold, and Michael Wraback

ARL-TR-5902 **January 2012**

NOTICES

Disclaimers

The findings in this report are not to be construed as an official Department of the Army position unless so designated by other authorized documents.

Citation of manufacturer's or trade names does not constitute an official endorsement or approval of the use thereof.

Destroy this report when it is no longer needed. Do not return it to the originator.

Army Research Laboratory
Adelphi, MD 20783-1197

ARL-TR-5902 **January 2012**

Heterogeneous Architectures Incorporating Nitride Semiconductors for Enhanced Functionality of Optoelectronic Devices (FY11)

Anand V. Sampath, Meredith L. Reed, and Michael Wraback
Sensors and Electron Devices Directorate, ARL

Michael Gerhold
U.S. Army Research Office

REPORT DOCUMENTATION PAGE	Form Approved OMB No. 0704-0188

PLEASE DO NOT RETURN YOUR FORM TO THE ABOVE ADDRESS.

1. REPORT DATE *(DD-MM-YYYY)*	2. REPORT TYPE	3. DATES COVERED (From - To)
January 2012	DSI	

4. TITLE AND SUBTITLE

Heterogeneous Architectures Incorporating Nitride Semiconductors for Enhanced Functionality of Optoelectronic Devices (FY11)

5a. CONTRACT NUMBER

5b. GRANT NUMBER

5c. PROGRAM ELEMENT NUMBER

6. AUTHOR(S)

Anand V. Sampath, Meredith L. Reed, Michael Gerhold, and Michael Wraback

5d. PROJECT NUMBER

5e. TASK NUMBER

5f. WORK UNIT NUMBER

7. PERFORMING ORGANIZATION NAME(S) AND ADDRESS(ES)

U.S. Army Research Laboratory
ATTN: RDRL-SEE-M
2800 Powder Mill Road
Adelphi, MD 20783-1197

8. PERFORMING ORGANIZATION REPORT NUMBER

ARL-TR-5902

9. SPONSORING/MONITORING AGENCY NAME(S) AND ADDRESS(ES)

10. SPONSOR/MONITOR'S ACRONYM(S)

11. SPONSOR/MONITOR'S REPORT NUMBER(S)

12. DISTRIBUTION/AVAILABILITY STATEMENT

Approved for public release; distribution unlimited.

13. SUPPLEMENTARY NOTES

14. ABSTRACT

Heterogeneous devices combine dissimilar materials with complementary device functionalities to achieve new functionalities that may provide revolutionary advances in technology. In these novel devices, the physics and engineering of the interface of the dissimilar materials plays a critical role and requires considerable research. This program investigates the heterogeneous integration of III-Nitride semiconductors with materials having dissimilar polarization, band gap, or crystal structure to realize optoelectronic devices that have enhanced capabilities not achievable using either material system individually. In the first year of this program, this effort has focused on four examples: (1) III-Nitride/silicon carbide (SiC) separate absorption and multiplication avalanche photodiodes, (2) III-Nitride/magnesium zinc oxide (MgZnO) hybrid near ultraviolet laser diodes, (3) heterogeneous III-Nitride terahertz optoelectronic devices, and (4) silicon solar cells incorporating a III-Nitride semiconductor active window.

15. SUBJECT TERMS

III-Nitride semiconductors, silicon carbide, SiC, MgZnO

16. SECURITY CLASSIFICATION OF:			17. LIMITATION OF ABSTRACT	18. NUMBER OF PAGES	19a. NAME OF RESPONSIBLE PERSON
a. REPORT	b. ABSTRACT	c. THIS PAGE			Anand V. Sampath
Unclassified	Unclassified	Unclassified	UU	44	19b. TELEPHONE NUMBER (*Include area code*) (301) 394-0105

Standard Form 298 (Rev. 8/98)
Prescribed by ANSI Std. Z39.18

Contents

List of Figures

Acknowledgments

We would like to acknowledge members of the Nitride Semiconductor Optoelectronics Team with the Sensor and Electron Devices Directorate for their contributions to this research program: Dr. Gregory Garrett (nitride/oxide laser technical lead and optical studies of the oxide/nitride laser diodes [LDs]), Dr. Grace Metcalfe (terahertz [THz] sources technical lead and optical studies of the indium gallium nitride [InGaN] materials), Dr. Paul Shen (technical consultation), Mr. Ryan Enck (molecular beam epitaxy [MBE] growth), Dr. Chad Gallinat (MBE growth), Dr. Nathaniel Woodward (optical evaluation of the InGaN THz sources), and Mr. Stephen Kelley (device fabrication). We also would like to acknowledge Professor Winston Schoenfeld's research group at University of Central Florida for the development of oxide semiconductors, as well as Professor Joe Campbell's group at University of Virginia for the fabrication and some characterization of the gallium nitride (GaN)/silicon carbide (SiC) avalanche photodiodes (APDs). We also thank Robert Ferrell and Professor Jim Speck of University of California at Santa Barbara for providing the InGaN cell material employed in the active window solar cell.

1. Introduction

Heterogeneous devices combine dissimilar materials with complementary device functionalities to achieve new functionalities that may provide revolutionary advances in technology. In these novel devices, the physics and engineering of the interface of the dissimilar materials plays a critical role and requires considerable research. While nitride semiconductors have had great success as materials for sources and detectors of electromagnetic radiation across the spectrum from ultraviolet (UV) to terahertz (THz), control of defect densities associated with the lack of suitable native substrates have kept the development of important devices such as avalanche photodiodes (APDs), lasers, and multi-junction, full-spectrum high efficiency solar cells in their infancy. On the other hand, there are other materials, such as silicon carbide (SiC), silicon (Si), and zinc oxide (ZnO), for which low defect density devices on bulk native substrates are possible, but they lack functionality for critical Army applications. SiC APDs are suitable replacements for photomultiplier tubes (PMTs) in UV communications systems employing the spectral range of their peak responsivity (260–280 nm), but their external quantum efficiency (QE) is dramatically reduced or nonexistent in the spectral ranges required for fluorescence detection (320–360 nm and 400–600 nm) and UV resonance Raman identification (230–260 nm) of biological agents and explosives. Si charge-coupled device (CCD) arrays are used for UV (240–260 nm) detection of hostile fire, but the sensitivity of even UV-enhanced, back-thinned devices is low in this spectral range. Moreover, Si solar cells remain the industry standard for high efficiency (~22%), low cost, large area energy harvesting applications, although manufacturable integration of Si cells with wider bandgap cells that could considerably boost efficiency for forward operating bases (FOBs) have yet to be realized. Finally, ZnO, magnesium oxide (MgO), and their alloys are among the most attractive materials for high efficiency UV sources required for purification, biodetection, and UV communications applications because of their high radiative efficiency associated with a large exciton binding energy and low defect density. However, while optically pumped UV stimulated emission and lasers based on ZnO, ZnO/magnesium zinc oxide (MgZnO) heterostructures, and ZnO nanowires have been demonstrated, there are no reliable electrically injected devices due to difficulties in p-type doping and concomitant hole injection.

While III-nitride semiconductors can be epitaxially deposited on all of these materials, this on its own will not address the limitations imposed by heteroepitaxial growth. Instead, this program focuses on developing heterogeneous devices combining Nitrides semiconductors with these dissimilar materials, having different bandgap energy, polarization, crystal structure, or other novel properties, to achieve new functionalities and leap ahead capabilities for the warfighter that cannot presently be achieved in either material system on its own. While there are a number of technologically important examples, during fiscal year 2011 (FY11) we focused on four

exemplary heterogeneous devices that can significantly enhance Army capabilities to demonstrate the utility of this approach. These examples include the following:

1. Polarization-enhanced gallium nitride (GaN)/SiC separate absorption and multiplication APDs
2. III-nitride/MgZnO near UV laser diodes (LDs)
3. Fiber-laser-pumped THz radiation sources based on inhomogeneous InGaN containing cubic domains
4. High efficiency Si solar cells employing a III-nitride active window

This report details technical achievements towards realizing these devices during FY11.

2. Polarization-enhanced III-Nitride/SiC Separate Absorption and Multiplication Avalanche Photodiodes

Reliance on the PMT detector currently inhibits the fielding of compact biological agent detection and/or identification systems on the Soldier level or in place-and-forget situations. The heterogeneous integration of a GaN absorption region and a SiC multiplication region holds promise for realizing highly sensitive and low-cost separate absorption and multiplication (SAM) APDs that can replace PMTs. The design shown in figure 1 has many advantages, which include the possibility of having high QE over a widely tunable spectral range from the visible to the deep UV by modifying the composition of the direct bandgap III-Nitride absorption region, as well as low dark current and high gain associated with the high quality SiC multiplication region. In addition, this device structure benefits from the formation of a type II heterojunction between the III-nitride and 4H-SiC layers with both the conduction and valence band energies of the GaN below those of the SiC and conduction band and valence band offsets that are between –0.6 and –0.9 eV and 0.7 and 1 eV, respectively (*1*). This band alignment promotes hole injection and inhibits electron injection from GaN into SiC, enabling single carrier injection of the photo-generated holes in the absorbing region into the SiC multiplication layer that is optimal since the hole ionization coefficient of SiC is much greater than that of the electron. As a result, these devices may have lower noise than SiC APDs.

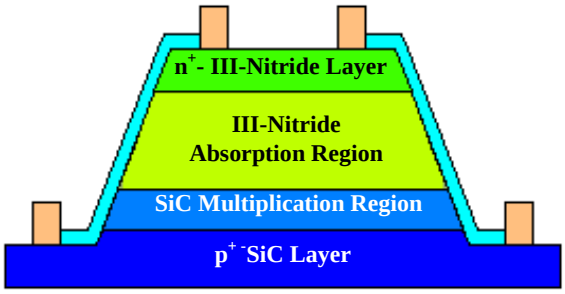

Figure 1. Device structure of a III-nitride/SiC APD.

This heterogeneous integration is achieved by heteroepitaxial growth of the III-nitride device layers by plasma assisted molecular beam epitaxy (PAMBE) on SiC epitaxial layers grown on 4H-SiC substrates. While heteroepitaxial growth of III-nitrides on SiC substrates has been demonstrated previously, it is important to appreciate that the SiC portion of the device plays a functional role in the device and is not simply a substrate. This heterointerface introduces interesting challenges that are unlike traditional heterojunction SAM APDs such as indium gallium arsenide (InGaAs)/indium phosphide (InP) telecommunications devices, including differences in spontaneous polarization as well as lattice mismatch that have important implications for device performance.

These detectors employ polar materials, with the SiC multiplication region having smaller spontaneous polarization than the III-nitride absorption region. While the positive polarization charge expected to form at the heterointerface between (In) GaN and SiC for III-face growth can achieve an optimal electric field profile in this device, a high field in the multiplication region of the structure desirable for high gain and a low field within the absorption region, insufficient or excessive charge can lead to poor performance. As a result, an additional method for controlling the density of interface charge is desirable.

Furthermore, InGaAs/InP APDs benefit from lattice matching of these materials as well as the ability to epitaxially grow the InP multiplication region and InGaAs absorption region directly on an InP substrate without interruption at the heterointerface; in this manner, the formation of deleterious defects can be prevented. In contrast, GaN has a 3.4% lattice mismatch with 4H-SiC that increases/reduces with indium nitride (InN)/aluminum nitride (AlN) mole fraction, resulting in the formation of threading dislocations that can act as leakage paths that increase dark current and prevent avalanche breakdown. While various heteroepitaxial buffer schemes have been developed for the growth of III-nitrides on SiC, these approaches must be modified or preferably avoided since the SiC region is not simply a substrate and the success of these devices hinges upon the efficient collection and injection of photogenerated holes into the SiC multiplication region.

2.1 Results

GaN/SiC SAM APDs were fabricated employing a 2-μm-thick p^+- SiC layer, a 480-nm-thick ν-SiC multiplication region, a 15-nm-thick magnesium (Mg)-doped GaN p-type interface charge control layer (PICCL), a 300–500 nm thick ν-GaN absorption region, and capped with a thin 10-nm-thick n^+-GaN layer so as to minimize absorption in this region. This device structure takes advantage of the positive polarization charge at the GaN/SiC heterointerface to obviate the need for a n-type SiC charge layer, while employing the Mg-doped GaN layer to control the magnitude of the interface charge for optimal performance. The GaN region of these devices were deposited directly on the 4H-SiC structure by PAMBE at a substrate temperature of 850 °C. Immediately prior to growth, the epilayer surface is cleaned in-situ by periodically covering the surface with gallium (Ga) metal and then allowing the metal to desorb. After wafer cleaning, mesas of various dimensions were defined by argon (Ar)/chlorine (Cl_2) inductive coupled plasma dry etching. A SiC sidewall bevel angel of ~7° was formed to prevent premature edge breakdown. A 290 nm-thick silicon dioxide (SiO_2) layer, which acted as both a passivation layer and an antireflective coating, was deposited by plasma-enhanced chemical vapor deposition. The p- and n-type contacts were formed by electron beam evaporation of titanium (Ti)/nickel (Ni).

Figure 2 shows the voltage dependence of the dark current, photocurrent, and photomultiplication gain for a 250-μm-diameter device. The device demonstrated dark current <1 pA for bias up to 90% of the breakdown voltage. The device-area and temperature dependence of the dark current were studied to determine the dominant component of the dark current. The dark current was fitted to the gain in the range 3 to 10 (reverse bias voltage of 148 ~ 151 V) for devices with diameters of 250, 180, and 130 μm. The multiplied dark current was proportional to the device area rather than the perimeter, an indication that the primary dark current is due to bulk leakage. Dark current densities were calculated to be between 1.0 ~ 1.5 nA/cm^2. This result suggests that the reverse leakage currents in these devices are limited by the SiC multiplication region despite the presence of threading dislocations at the heterointerface. It is also important to note that the dark current in these devices is ~1000 times lower than what has been observed for GaN APDs despite having areas that are up to ~25 times larger (*2*).

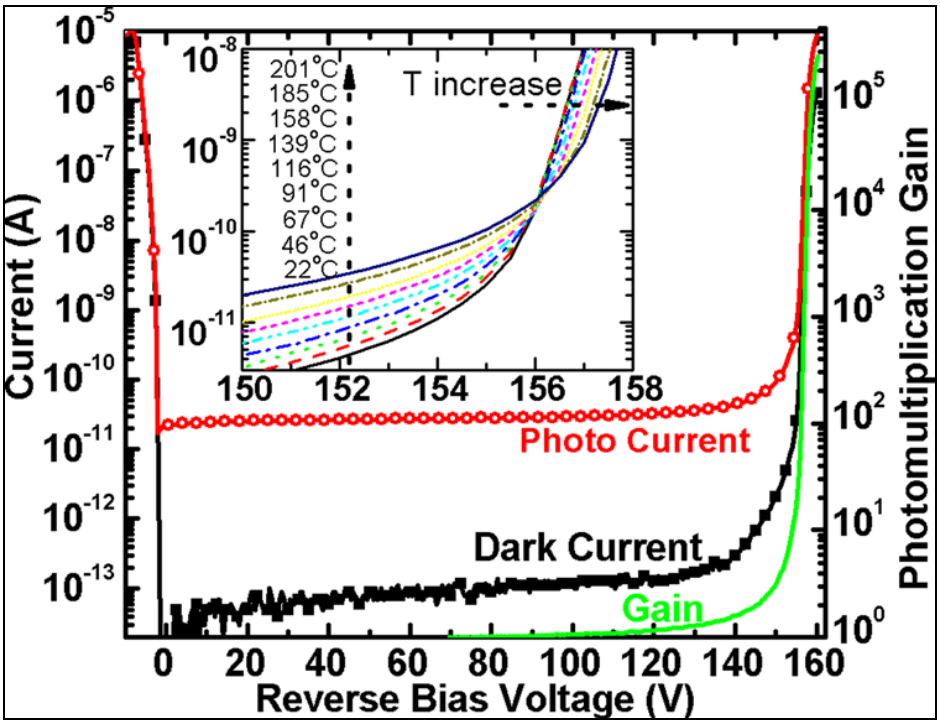

Figure 2. Measured dark current (black), photocurrent (red) and gain (green) for a GaN/SiC APD. Temperature dependent current-voltage (I-V) characteristics (inset).

The inset of figure 2 shows the dark current of a 250-μm-diameter device at temperatures from room temperature to 201 °C. A positive temperature dependence of the breakdown voltage was observed, an indication that breakdown is caused by avalanche multiplication. The breakdown voltage temperature coefficient was ~0.05 V/°C. From Arrhenius plots of current in the voltage range of between 140 and 150 V, low activation energies of ~0.1 eV were determined. This may indicate high levels of shallow level traps, which could be the result of high defect densities at the GaN/SiC interface.

The photocurrent was measured while the device was illuminated by a broad-spectrum xenon (Xe) UV lamp. The photomultiplication gain was calculated by dividing the photoresponse at a given voltage by the unity gain photoresponse. Here the unity gain was arbitrarily chosen at a 70-V reverse bias where the photocurrent is relatively independent of voltage. We note that the calculated gain based on the reported impact ionization coefficients (*3*) is less than 1.05 at 70 V for this structure. A maximum gain $>10^5$ was observed before the photocurrent reached the compliance current (1 μA) at reverse bias of 160 V.

Further insight into the voltage-dependent photocurrent can be gleaned from spectral responsivity data. The spectral responsivity was measured by comparing the response of the device under test with that of a calibrated Si reference photodiode. A Xe lamp and monochromator were used as the narrow spectrum light source from 300 to 400 nm. Figure 3 shows the measured responsivity versus wavelength at several voltages (open points). The

spectral response at bias less than ~150 V is characterized by a local maxima at ~374 nm and a local minima at 366 nm that is neither consistent with the collection of carriers generated in the GaN absorption region nor with the response of a simple SiC APD. Modeling accounting for the GaN absorption (black solid line) and the response of a wholly SiC detector indicates that the peak at 374 nm is due to the reduced absorption in the GaN region resulting in more light passing through the GaN layer and reaching the SiC layer, indicating that the photoresponse is from the collection of carriers generated directly in the SiC multiplication region with the GaN absorption layer acting as an optical filter (blue dash line). The lack of GaN-related response at low bias voltage is likely due to the confinement of the electric field within the SiC multiplication region and the concomitant low probability of photogenerated holes diffusing through the highly defective GaN/SiC interface to the SiC multiplication region. For a bias below 90 V, there is almost no change of the responsivity, indicating there is no gain in the SiC multiplication layer.

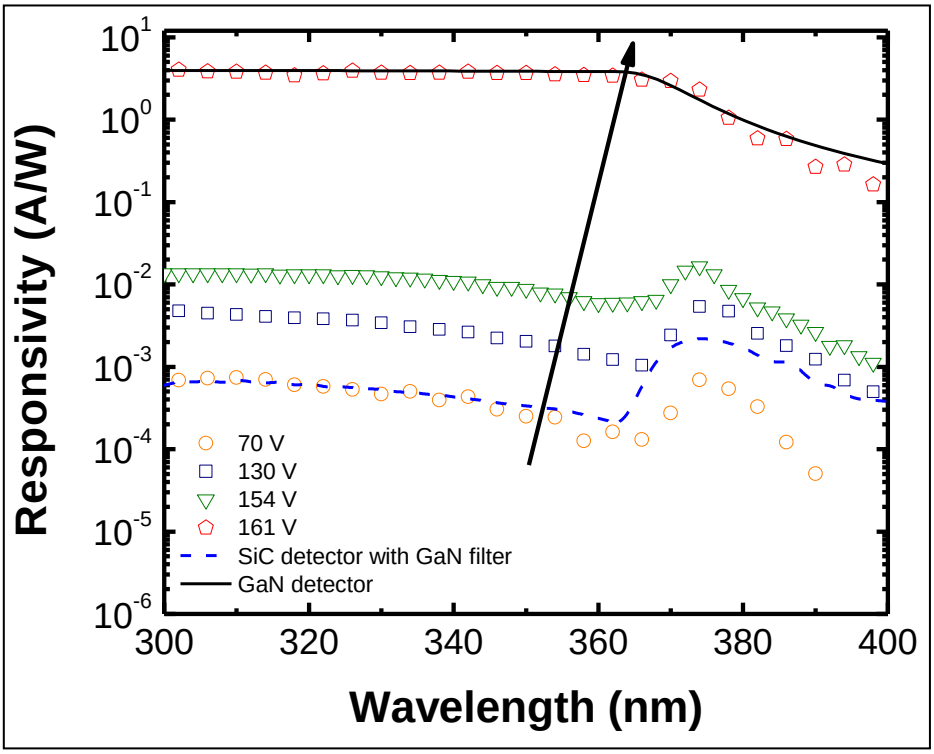

Figure 3. Measured responsivity of GaN/SiC APDs (open shapes), typical response from a GaN detector (black), and the calculated response of a SiC detector through a GaN filter.

The responsivity starts to increase for a bias of about 130 V, but the spectral shape remains unchanged until the bias exceeds ~150 V (not shown), indicating that there is no injection of holes from the GaN region up to this point. Above 154 V, the device begins to exhibit photoresponse that is clearly associated with the collection of carriers generated in the GaN absorption region. This transition in the photoresponse is attributed to the punch through of the electric field into the GaN absorption region and its gradual rather than sharp depletion with increasing bias, leading to the sweepout of the photogenerated holes into the multiplication

region. Finally, at 160 V, the spectra exhibit a GaN response. A peak responsivity of 4.2 A/W was achieved at a reverse bias of 160 V. The cut off wavelength of the responsivity shifted from ~380 nm at a 70-V reverse bias to ~400 nm at 150 V. This responsivity is significantly larger than what has been reported for GaN APDs (*2*) and can be attributed to the larger gain achieved in the SiC multiplication region. The transition from SiC dominated response at low reverse bias to GaN dominated response at high bias indicates that the gain calculated from the I-V characteristics in figure 2 is not purely the avalanche multiplication gain as the difference in effective photon flux on the disparate absorption regions for different biases has not been accounted for.

3. III-nitride/MgZnO Near UV Laser Diodes

UV sources are required for current Army programs related to biological threat detection as typified by the next generation tactical-biological (TAC-BIO) sensor under development by Edgewood Chemical and Biological Center (ECBC). The brighter these sources, the more robust and useful the detection system, but currently for light-emitting diodes (LEDs) based on aluminum gallium nitride (AlGaN), increased output power can only be achieved through lamps designed with larger emitting areas that cannot be tightly focus to increase photons on target. Replacement of these LEDs with UV semiconductor LDs, with their higher power and directional output, would greatly broaden the utility of these biodetection systems. Development of UV LDs would also provide access to a new spectral source range for Army programs in standoff detection, optical remote sensing technology (light detection and ranging [LIDAR]), and covert communications. LD sources emitting at 355 nm are of particular interest as they can directly replace existing frequency tripled, bench top, neodymium (ND): yttrium aluminum garnet (YAG) layers currently used by system designers.

AlGaN and MgZnO semiconductors are two families of wide direct bandgap materials that are attractive for fabricating compact deep UV laser sources as their bandgap can be tuned to the region (wavelength) of interest by controlling the mole fraction of AlN to GaN in the III-nitride or of the MgO to ZnO in the II-oxide semiconductor. $Al_xGa_{1-x}N$ has a wurtzite crystal structure and growth has been demonstrated along the entire ternary range, but is traditionally deposited on sapphire substrates, which leads to strain management problems, the generation of a high concentration of defects, and eventually, cracking. In contrast, ZnO also grows in a wurtzite structure but MgO grows preferentially in a cubic orientation and growth of wurtzite $Mg_yZn_{1-y}O$ has only been demonstrated up to $y \cong 0.36$, after which MgO begins to segregate into cubic clusters (*4*). MgZnO devices are expected to be brighter and more efficient than AlGaN devices due to their higher exciton binding energy and faster, more efficient radiative recombination. High quality (low structural defect) bulk ZnO is also available for ZnO homoepitaxial growth, which should provide high quality material with low defect densities, and thus, low loss. Also,

the homoepitaxial growth provides easily aligned cleavage planes for producing mirror-like end facets for a laser cavity, something not possible for growth on sapphire.

Despite these points that suggest MgZnO would make a better device at wavelengths longer than 300 nm, AlGaN is the current material system of choice for production of UV optoelectronics because there are no efficient *p*-dopants for these materials currently. In contrast, *p*-doping is possible for GaN, the most common dopant being Mg, and growth of quality *p*-layers for electrically injected devices has been routinely demonstrated in our lab with free hole concentrations at the high 10^{17} cm^{-3} level. Yet while heroic efforts have produced laboratory examples of 340-nm AlGaN-based LDs (*5*), no LDs emitting at wavelengths shorter than 370 nm are commercially available due to aforementioned problems with AlGaN growth.

A promising solution is to develop a heterogeneous device through the growth of high mobility *p*-doped (Al)GaN layers with high efficiency MgZnO-based LD active regions so as to incorporate the best aspects of the two dissimilar material systems with the goal to create rugged, compact, and high efficiency 355-nm semiconductor lasers for Army applications. This is accomplished through the heteroepitaxial growth of *p*-(Al)GaN layers by PAMBE on high quality MgZnO active regions to produce efficient LDs. A typical LD structure consists of a *p*-*i*-*n* structure where holes (*p*) and electrons (*n*) are injected into an intrinsic (*i*) active region where they recombine to give light at the desired wavelength (figure 4). LDs are laterally emitting slab structures that require a high quality intrinsic region, typically a multi quantum well (MQW), that exhibits low absorption and can support higher currents.

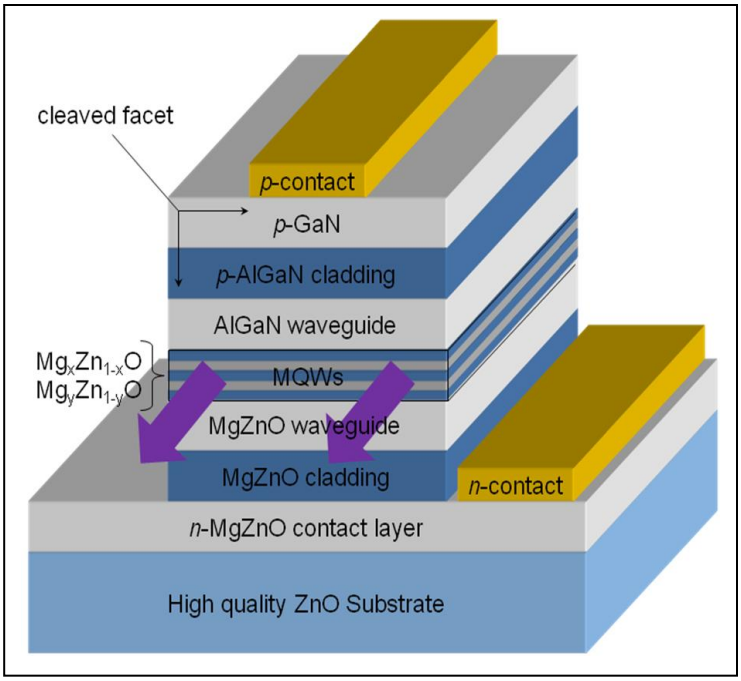

Figure 4. Schematic of a MgZnO/AlGaN LD that employs a MgZnO electron injection and MQW active region and an AlGaN/GaN hole injection region, all grown on a bulk ZnO substrate.

3.1 *n*-ZnO Active Region Development

A significant advantage of this approach is the increasing commercial availability of high-quality bulk ZnO crystal substrates for homoepitaxial oxide growth, with dimensions (1 cm^2) and price points ($300) significantly better than that currently available from the bulk GaN industry. With no (Mg)ZnO growth infrastructure at the U.S. Army Research Laboratory (ARL), a cooperative agreement with Dr. Winston Schoenfeld at the University of Central Florida (UCF) was entered into where they would purchase bulk ZnO substrates and grow MgZnO active regions for this project. Tokyo Denpa Co., Tokyo, Japan, was picked as the bulk ZnO substrate provider due to its observed better quality (*6*) of their material. Dr. Schoenfeld's group also used PAMBE growth techniques and synergy was expected with our PAMBE growth team. To achieve high electron mobility in the ZnO LD structures, impurity doping of Ga was used to increase the free electron concentration. Optical spectroscopy and Hall Effect measurements were to be used to qualify the effectiveness of the Ga-doping.

Deposition of the ternary MgZnO system was expected to be more difficult, so a gradual approach of slowly increasing the Mg content of the $Mg_{1-y}Zn_yO/Mg_{1-x}Zn_xO$ MQW active region was to be employed with the goal of getting as short a wavelength as possible in the given time and material constraints of the project. Ga-doping was correspondingly expected to be less efficient in the ternary system. Analytical feedback was provided to help optimize the growth and time-resolved spectroscopy was used to study the carrier dynamics in the device active region as the program progressed.

3.2 *p*-GaN Layer Growth

Although growth of high mobility *p*-GaN had been demonstrated by our III-nitride PAMBE growth group before, transition of these techniques to growth on ZnO was identified as the main challenge of this project. The only practical impurity dopant to increase the hole concentration in the *p*-GaN layer is interestingly Mg, which was used in this study. Whereas heteroepitaxial growth of GaN devices allows for a graduated deposition process with buffer layers and graded layers that move the active region away from a defective heterointerface, the heterointerface between the *p*-GaN and ZnO active region needed to be a clean transition to allow efficient carrier injection vertically across the junction and to minimize optical scattering and loss in the horizontal direction of the LD resonator.

ZnO has a low thermal stability that presents problems in the traditional III-nitride PAMBE growth environment. ZnO thermally decomposes in vacuum at temperatures higher than ~650 °C while III-nitride PAMBE growth temperatures optimally occur in a range from ~500 °C for InN growth to ~1000 °C for AlN, as outlined in figure 5. GaN growth is typically optimized at ~720 °C for undoped and Si-doped (*n*-type) layers while Mg-doping (*p*-type) can be achieved at the slightly lower growth temperature of ~650 °C. In addition to ZnO's relatively low thermal stability, zinc (Zn) readily diffuses out off ZnO under the presence of liquid Ga coverage on the ZnO surface. The resulting Ga-Zn alloy and defective ZnO layer would degrade the

p-GaN/*n*-ZnO heterojunction and subsequent *p*-GaN epilayer growth. Thus, temperature and Ga flux were identified as the main variables for optimizing the deposition of a quality *p*-layer.

With increasing bandgap of the MgZnO LD structure, it was envisioned that the bandgap of the *p*-GaN layer would need to be increased by changing to a ternary *p*-AlGaN layer. This would introduce two new material compositions where the growth interface would need to be optimized but with hopefully minor, linear corrections.

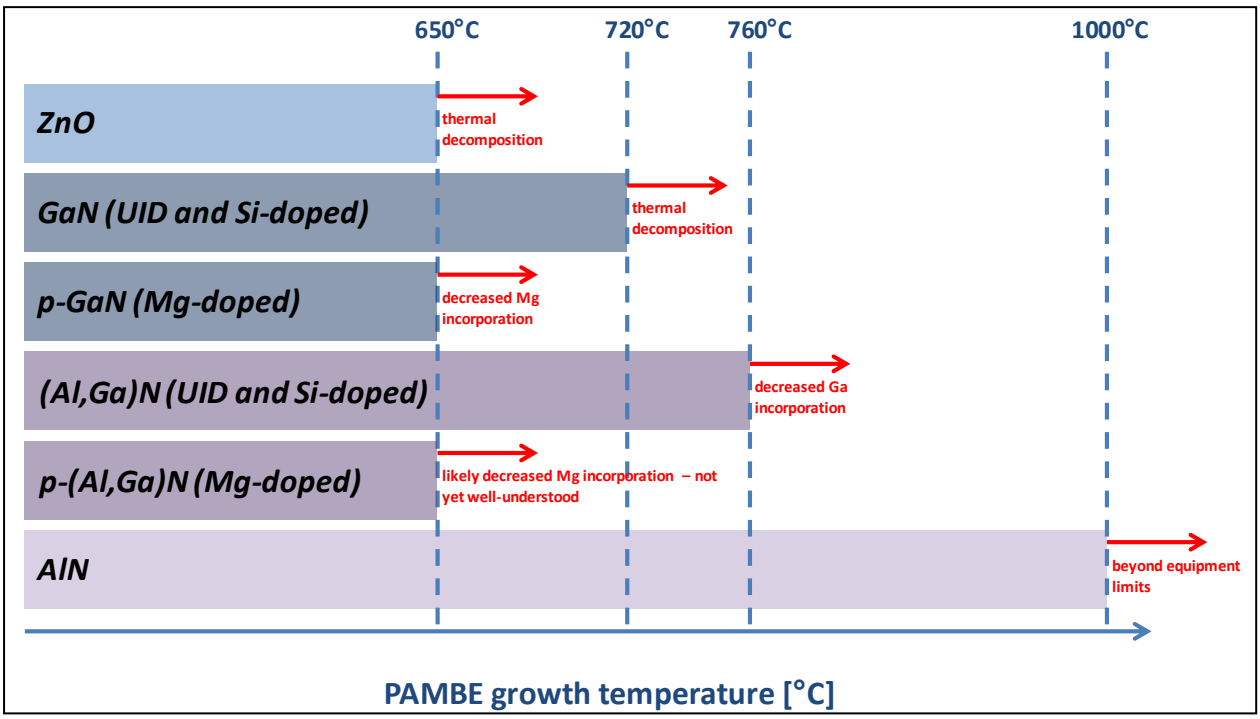

Figure 5. Growth temperature and thermal decomposition temperature comparisons for ZnO and the relevant III-nitrides. GaN and (Al,Ga)N have optimized structural and morphological properties when grown just below their thermal decomposition temperatures. Sufficient Mg-doping occurs at growth temperatures much lower than thermal decomposition temperature—sacrificing structural and morphological quality for *p*-type doping.

3.3 Results

Two lots of 12 *c*-plane, 1 cm^2, bulk ZnO substrates have been received from Tokyo Denpa by UCF and of these, one substrate was sent to ARL for characterization. UCF has sent five of these samples with homoepitaxial growth of ZnO and one with Ga:ZnO (*n*-doped) for characterization and *p*-GaN regrowth. Included with the bulk ZnO samples were half wafers of ZnO and Ga:ZnO grown on 2-in sapphire for calibration/practice runs of the *p*-GaN growth.

3.3.1 *n*-ZnO Active Region Development

Homoepitaxial growth of ZnO was first tried on the Zn-polar surface of the ZnO substrates with the optimized conditions identified for heteroepitaxial growth of ZnO on sapphire. The growth rate was found to be three times faster than growth on sapphire, leading to rough, three-

dimensional growth. Not unexpectedly, the surface mobility and growth kinetics of homoepitaxial ZnO were different than that on sapphire. It had been previously shown that growth is preferred under O-rich or stoichiometric conditions on bulk ZnO substrates. This achieves smooth layers and it was found that the sample temperature needed to be increased from 500 to 700 °C to achieve improved surface morphology and terraces, as shown in figure 6. The smooth morphology was emphasized as variations need to be less than the thickness of the individual wells in the MQW active region.

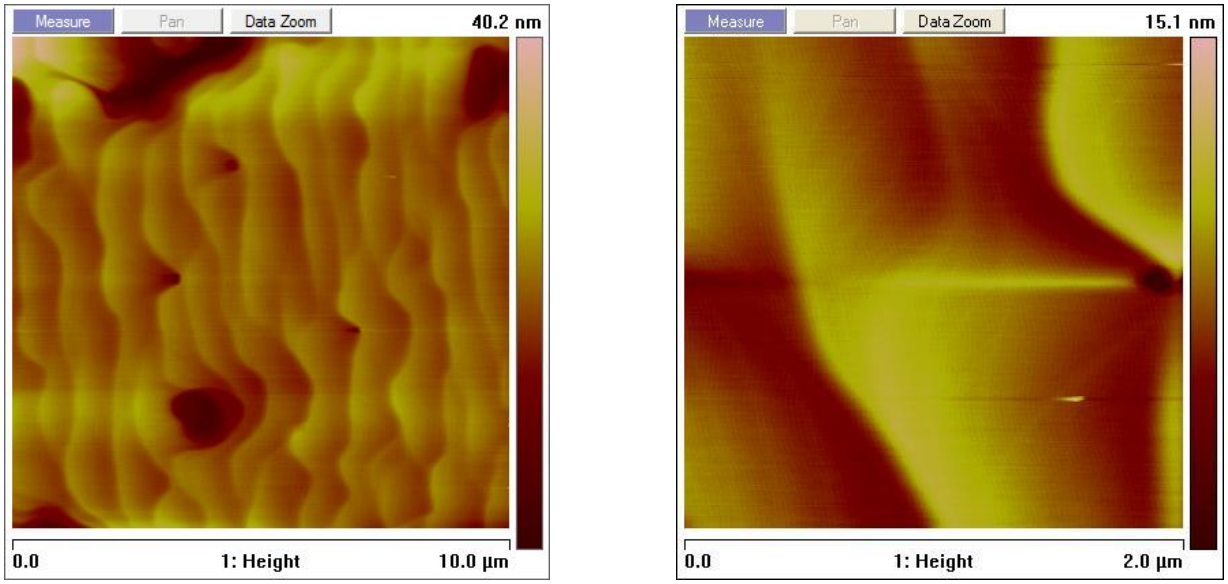

Figure 6. Atomic force microscopy (AFM) images of ZnO on bulk ZnO with *c*-plane 0.5° miscut to *m*-plane. The roughness for the 2-µm feature is 1.94 nm. Best samples achieved root mean square (RMS) values down to 0.139 nm for 1 μm^2.

For better heat conduction, homogeneity, and more uniform growth, a Ti deposition on the back side (O-polar face) of the ZnO substrate was implemented. This would also align the ZnO growth more closely with the traditional GaN PAMBE growth at ARL where the substrate backside is coated. With the coating, it was possible to maintain a smooth morphology with reduction in the growth temperature down to 600 °C. But in the end, it was found that the Ti back-coating was reacting with the oxygen-rich growth conditions and that the Ti was being incorporated into the front ZnO homoepitaxy leading to a probable zinc titanate ($ZnTiO_3$) cluster and out of band emission. At this time, it was also noted that there was a variation in the miscut of the bulk ZnO templates across the purchased lots and the difference in viscinality was leading to varying morphology and needed to be monitored. Active region development was continued with optimization of *n*-type Ga:ZnO deposition on the ZnO for the electron injection layer. As found by Hall Effect measurements, electron concentrations up to $1.6\times10^{18}/cm^3$ were achieved. The introduction of Ga into the growth process was also found to improve the morphology of the homoepitaxy growth, resulting in surface quality better than the original bulk substrates and

giving RMS values down to 0.10 nm. Unfortunately photoluminescence (PL) studies (not shown) do not reflect an increased light emission.

Concurrent with development of ZnO on bulk ZnO, optimization of MgZnO growth on sapphire was performed to identify stable growth conditions. Growth with 9% Mg concentration has been demonstrated with RMS values of 0.366 nm, maintaining the smooth interface required for use in heterojunction growth. N-type doping of the MgZnO was demonstrated for carrier concentrations up to $9.36\times10^{18}/cm^3$ and mobilities of 150 $cm^2/V\text{-}s$.

3.3.2 *p*-GaN Layer Growth

Growth of *p*-GaN on sapphire was demonstrated at temperatures as low as 600 °C with carrier concentrations in the mid-10^{17} and the Mg incorporation in was found to decrease significantly at growth temperatures beyond 650 °C. Initial *p*-GaN/ZnO epilayers were optimized on the PAMBE grown ZnO on sapphire substrates provided by UCF. We monitored the reflection high energy electron diffraction (RHEED) signal and the mass spectrum of thermally desorbing atomic species by residual gas analysis (RGA) to ensure the ZnO did not thermally decompose during heating prior to *p*-GaN deposition. The RHEED pattern did not change nor were any desorbing species (Zn or O) observed up to 650 °C, indicating the ZnO was thermally stable in the desired growth temperature window.

The wurtzite structure of both ZnO and the III-nitrides has an internal polarization along the *c*-axis, perpendicular to the growth plane of our device. This polarization field has been shown to help with *p*-type carrier transport when the *p*-layer is on the metal (Zn or Ga)-polar face (*7*), which is the case for this project. Mg is known to flip the polarity of GaN from Ga-polar to N-polar under insufficiently Ga-adlayer coverage during PAMBE growth. This polarity inversion would lead to poor material quality. Typically, high-quality *p*-GaN growth with no polarity inversion is achieved under a Ga-rich surface between 1 and 2.5 monolayers of Ga-adlayer coverage but this could lead to diffusion of Zn atoms from the ZnO crystal into the liquid Ga as discussed earlier. We studied the effect of different GaN growth nucleation procedures on the surface morphology of *p*-GaN grown on ZnO/sapphire. The two nucleation schemes studied were the following:

1. The typical nucleation method in which we first deposited 2.5 monolayers of Ga prior to active nitrogen and Mg exposure. This ensured a complete Ga wetting layer avoiding a “dry” GaN surface and the possibility of surface polarity inversion.

2. A “dry” nucleation method in which we first nitridated the ZnO surface by exposing the sample to the active nitrogen species prior to Ga or Mg deposition. After a variable nitrogen exposure, we started GaN growth with a Ga flux lower than the active nitrogen species, N-rich growth, and then ramped up the Ga flux to achieve Ga-rich growth conditions prior to initiating Mg doping.

Figure 7 shows the surface morphology as observed in scanning electron microscopy (SEM) for the starting ZnO surface and the final *p*-GaN surfaces for samples grown using nucleation scheme 1 or scheme 2 with a 10-min nitridation interval. Method 1, nucleating with a Ga-wetting layer, resulted in poor surface morphology with significant voids and an incomplete epilayer. GaN nucleation using the nitridation and subsequent Ga flux ramp of method 2 realized completely coalesced GaN epilayers and smooth surface morphology. Decreasing the nitridation time yielded similar surface morphologies and even eliminating the nitridation and proceeding directly to nucleation with an N-rich Ga flux and subsequent ramp provided good results, but transmission electron microscopy (TEM) of the interface is needed to confirm the uniformity of the interface layer where the Ga is introduced. The thickness of this layer without Mg doping will influence the *p*-mobility of the device, but as described in reference 24, material polarization will be helping.

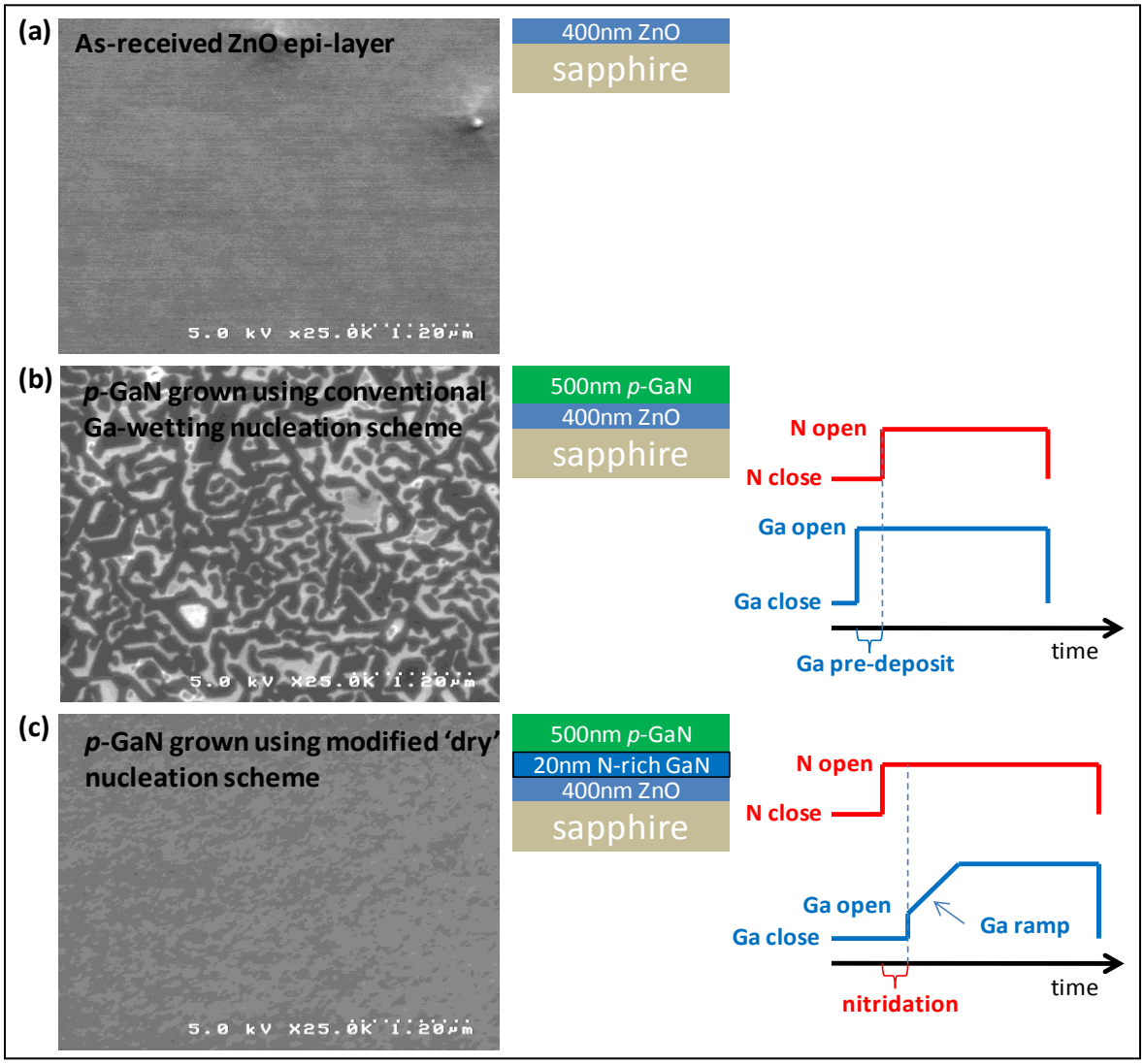

Figure 7. (a) SEM of an as-received ZnO (Zn-polar) epilayer on sapphire, (b) a *p*-GaN layer grown on ZnO/sapphire using the conventional Ga-wetting nucleation technique (method 1), and (c) a *p*-GaN layer grown using the "dry" nucleation technique (method 2).

PL of the active region emission in a ZnO on sapphire sample before and after growth of a *p*-GaN layer was taken and found to show no decrease in the signal strength, indicating no noticeable degradation of the active region. In fact, a slight increase in the PL admission was observed, which could indicate a reduction of the surface field at the ZnO/*p*-GaN interface as compared to the bare ZnO with higher surface fields, which can reduce recombination efficiency.

Observing a diode response in the *p*-GaN/*n*-ZnO structure is the best way to confirm quality *p*-GaN deposition, and measurement of the *p*-carrier concentration by Hall Effect is only possible in a multilayer structure if it exhibits diode characteristics with an insulating depletion region between the *n*-layer and *p*-layer. To check for successful *p*-doping of the GaN layer and also as a check of the junction quality, the sample from figure 7c was processed into a diode test structure using standard ZnO methods from literature. The diodes were found to be weakly rectifying but SEM images of the devices showed the contacts and metallization were not optimal with shorting occurring. Optimization of the processing is being pursued.

While structural feedback during growth optimization did lead to improved planar structures with low structural defects, time-resolved optical spectroscopy showed that the recombination dynamics were far from efficient. With PL lifetimes for these materials much shorter than that seen in non-polar growth (not shown), an easier growth plane but one not compatible with employing polarization-enhanced *p*-doping design, future work must now focus on decreasing the non-radiative carrier lifetimes to improve light emission efficiency. The most probably explanation for poor lifetimes is a high point defect density. Identifying the nature and source of these defects is a priority.

Carrier confinement in a MWQ active region will also improve lifetimes and the next step in growth on bulk ZnO substrates will be perfecting MgZnO/ZnO quantum well growth that is *optically bright*. Development of the *p*-doped layer would then shift to ternary AlGaN with emphasis on maintaining a quality electrical junction. Recent publications (*8*) have confirmed that the valence band off-set of AlN (0.43 eV) is much smaller than GaN (1.37 eV) relative to the valence band of ZnO. This energy represents a barrier to hole injection into the MgZnO/ZnO MQW. It has been decided that the polarization enhanced *p*-doping would thus benefit from initiating the *p*-layer growth with AlN and grading down to GaN as shown in figure 8. Final success will be defined by a device that is over and order of magnitude more efficient than an equivalent all III-nitride structures in light emission.

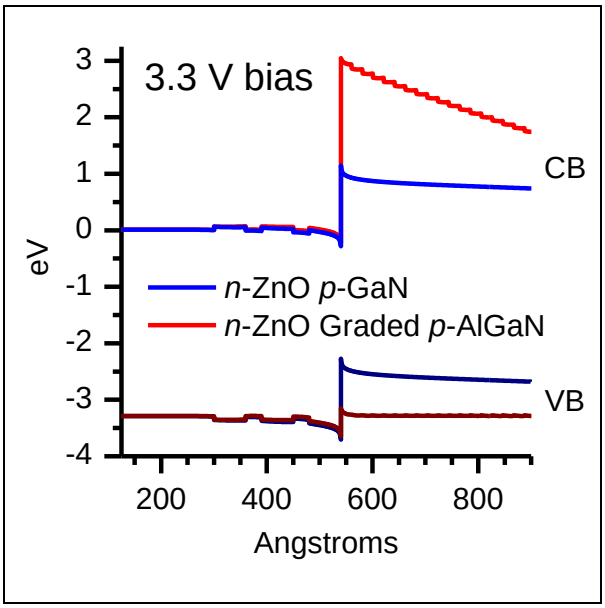

Figure 8. New *p*-doping structure to reduce the barrier to hole injection introduced by the valence band offset of III-nitrides relative to that of ZnO (valence band maximum [VBM]). The larger relative conduction band offset (CBM) of AlN acts as a beneficial electron blocking layer.

4. Fiber-laser-pumped THz Radiation Sources Based on Inhomogeneous InGaN Containing Zincblende Domains

Since the bandgap of AlN, GaN, and InN and its alloys spans the UV through infrared (IR) wavelength range, III-nitride-based THz devices can be engineered to operate at fiber-laser wavelengths for low-cost, compact, field-deployable THz systems leveraging fiber-optic technology. These systems will have a number of applications including standoff explosive detection and vision through obscurants. Recently, we observed enhanced THz generation due to large stacking-fault (SF) related internal in-plane electric fields (figure 9) in *m*-plane GaN thin films (*9*). The SFs are thin zincblende inclusions in an otherwise wurtzite crystal structure and form due to heteroepitaxial growth of non-polar GaN on lattice-mismatched substrates. The strong internal, in-plane polarization of the wurtzite crystalline structure is terminated at the wurtzite/zincblende interface, where charge accumulation leads to strong electric fields within the wurtzite domains that point in the same direction (along the *c*-axis of the crystal), effectively creating an array of contactless photoconductive (PC) switches. In-plane transport of carriers generated under ultrashort pulse excitation proceeds parallel to the electric field, leading to a THz radiation component polarized preferentially along this axis of the sample. The built-in field is estimated to be ~290 kV/cm in the wurtzite region of *m*-plane GaN with a SF density of ~$1x10^6$/cm.

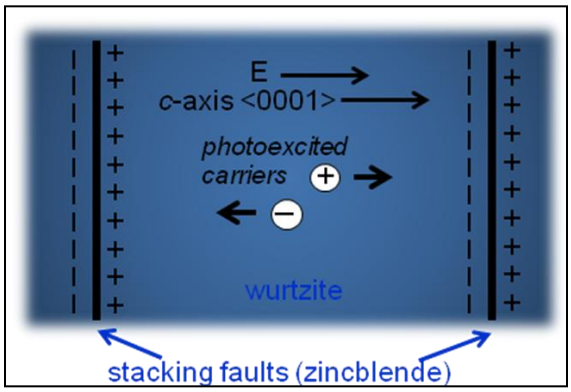

Figure 9. Schematic of in-plane electric field due to stacking faults in nonpolar or semipolar nitride material.

Due to built-in lateral SF-related fields, non-polar and semi-polar InN or InGaN are ideal as THz sources operating near fiber-laser wavelengths (1030 and 1550 nm). Recently, non-polar InN was investigated and showed similar SF-related fields (*10*). Unfortunately, the best quality InN and high In-fraction InGaN still have high unintentional doping (UID) concentrations, which can screen the THz field (*12*). Small In-concentration $In_xGa_{(1-x)}N$ ($x<0.3$), however, has a UID concentration low enough such that *p*-doping is possible. By using $In_xGa_{(1-x)}N$ material with a bandgap engineered near 515 nm ($x\sim0.26$), the doubled frequency of a compact femtosecond fiber laser could be used.

The internal in-plane electric fields in non-polar and semi-polar nitride materials also imply a method of *detecting* THz fields by modulating the exciton absorption through excitonic electroabsorption without an external bias. The nitride-based THz detector also has advantages over conventional semiconductor THz detectors in that it does not require electrode processing as in photoconductive switches, or phase-matching as in electro-optic (EO) crystals. In the excitonic electroabsorption effect, the electric field ionizes excitons and produces anisotropic bleaching of the anisotropic absorption (figure 10). The excitonic electroabsorption effect has been observed in materials such as GaAs MQWs (*13*) and is the basis for various optical devices including optical modulators, switches, and photodetectors.

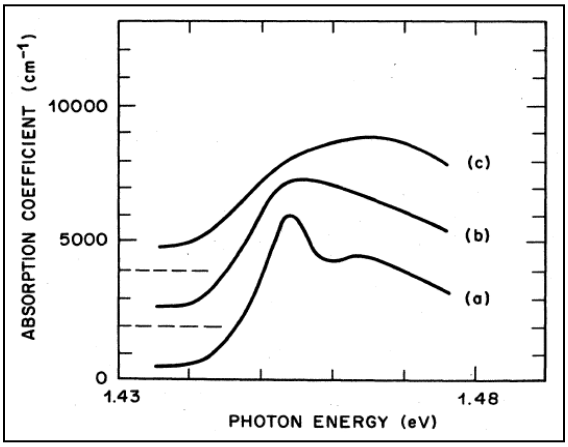

Figure 10. Absorption spectra at various applied electric fields parallel to GaAs MQWs (*13*).

THz fields are usually relatively small (<10 V/cm) and would produce an almost vanishing excitonic electroabsorption response. However, by using a large static electric field, similar to the internal field in non-polar and semi-polar nitrides, incident THz radiation could modulate the static field, producing an anisotropic change in the anisotropic absorption, and be detected using lock-in techniques. Coherent detection of free-space THz electrical transients has already been demonstrated using the excitonic electroabsorption effect in GaAs MQWs and applying a lateral bias field (*14)*. The DC field to maximize the GaAs detector sensitivity was found to be 8 kV/cm. One advantage of using non-polar and semi-polar nitride semiconductors for THz detection is that no external bias field would be required as in the GaAs device. In addition, in reference 14 the difference in anisotropic absorption, and therefore THz field, was measured using amplitude modulation of a probe beam. For a higher sensitivity measurement, polarization rotation of a probe beam (figure 11) can be used instead to measure the incident THz field (*15*).

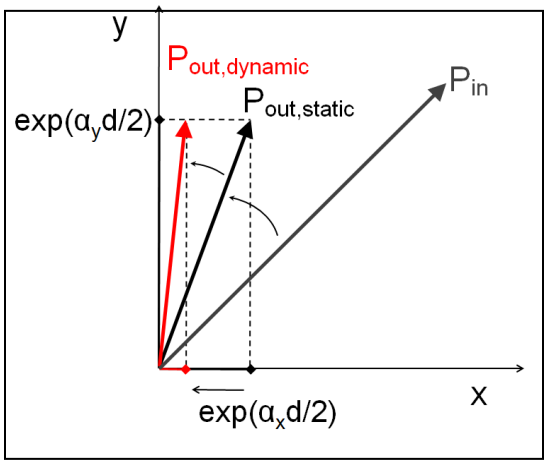

Figure 11. Illustration of probe polarization rotation due to anisotropic absorption in static and dynamic field.

Furthermore, an optical anisotropy in the semiconductor, resulting from a lowering of the crystal rotational symmetry by uniaxial strain as in GaAs or using a non-polar orientation as in wurzite materials, would allow for an even more sensitive method of sampling the THz electric field. The optical anisotropy can be enhanced by strain, which modifies the electronic band structure and enhances the absorption anisotropy to as large as $\Delta\alpha=\alpha_{\perp}-\alpha_{\parallel} \approx 5\times10^{4}$ cm^{-1}, with $\Delta\alpha/\alpha$~0.7 in GaN. Significant polarization rotation of as much as 36° of a probe beam has been demonstrated in strained *m*-plane GaN at room temperature (*16*).

4.1 Results

In the first year of our project, we successfully developed a heterogeneous nitride-based THz source operating at 400 nm using ARL-grown *a*-plane InGaN. We also implemented ARL-grown *a*-plane GaN and $In_xGa_{1-x}N$ with x~5–9% for a bandgap near 400 nm for THz detection.

4.1.1 Material Growth

For efficient THz emission and detection, a high density of SFs resulting from growth on lattice mismatched substrates is necessary. We achieved growth of *a*-plane InGaN epitaxial layers on double-sided polished *r*-plane sapphire using a Veeco Modular Gen II molecular beam epitaxy (MBE) reactor. High quality growth of *a*-plane InGaN involves precise control over several growth parameters, including growth temperature and the relative arrival rate of group III and group V atoms to the surface. Although the growth conditions for *c*-plane InGaN material can serve as a guide, optimization must be performed for *a*-plane growth since In incorporation, ideal growth temperature, and growth kinetics change with crystal orientation.

Firstly, growth of single crystal InGaN epitaxially on *r*-plane sapphire requires the development of a suitable nucleation material as well as an appropriate buffer layer material to ensure high quality InGaN. Guided by the nucleation material used in *c*-plane growth, we grew an *a*-plane GaN buffer layer on either low-temperature (~600 ºC) grown GaN or high-temperature (~800 ºC) grown AlN. Characterization of the resulting films by AFM and double crystal x-ray diffraction revealed that growth on the low-temperature-grown GaN nucleation layer yielded a higher quality, lower surface roughness GaN buffer layer.

Next, we optimized the GaN buffer layer, which provides a low lattice mismatched surface for the growth of InGaN. The buffer layer deposition transitions from a three-dimensional growth mode to a two-dimensional step-flow growth through the coalescence of the nucleation sites at the sapphire-GaN interface (known as Stranski-Krastanov growth). The GaN buffer layer also isolates the InGaN epilayer from any oxygen that may diffuse from the sapphire substrate. Isolation of the InGaN from substrate surface contaminants and the effusion of oxygen is especially important for THz detection since screening effects due to the resulting background carriers will lower the THz detection efficiency. Deposition of the GaN buffer layer was optimized using a series of Ga flux and growth temperature adjustments and *in situ* monitoring using RHEED and pyrometer temperature measurements. A high quality *a*-plane GaN buffer

layer was ultimately obtained using a two-step growth process, a Ga flux of 2.1×10^{-7} Torr, and a thickness of 500 nm atop the low-temperature-grown GaN nucleation layer to provide sufficient isolation from the sapphire substrate. Excellent surface morphology (surface roughness of 8.8 nm) of the GaN buffer was verified using AFM (figure 12).

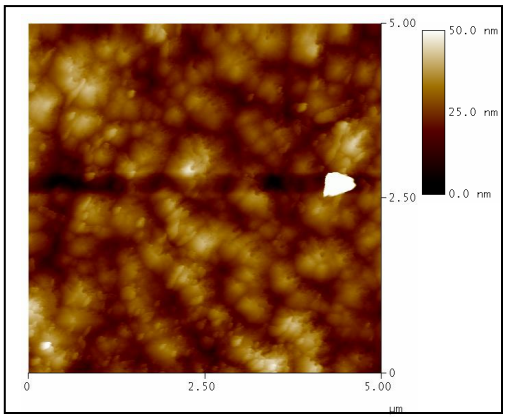

Figure 12. AFM image showing excellent surface morphology of the *a*-plane GaN buffer layer grown by MBE.

To determine the process window for the growth temperature of *a*-plane InGaN, we grew a series of samples, each at a lower substrate temperature until saturation of the In content occurred. We then adjusted the Ga flux to limit the In content to approximately 7.8% for a bandgap near 400 nm. Once we achieved saturation, the surfaces of these samples were compared to determine which growth temperature led to the smoothest surface. After determination of the relative Ga flux and growth temperature, a series of growths were performed to determine the minimum In flux necessary to grow stoichiometric InGaN without the accumulation of In droplets, which lead to droplet-related defects. The highest quality *a*-plane InGaN films were grown at a temperature of 575 °C, a Ga flux of 1.8×10^{-7} Torr, and an In flux of 2.1×10^{-7} Torr. X-ray diffraction data of the film confirms an In concentration of ~ 5–9% (figure 13).

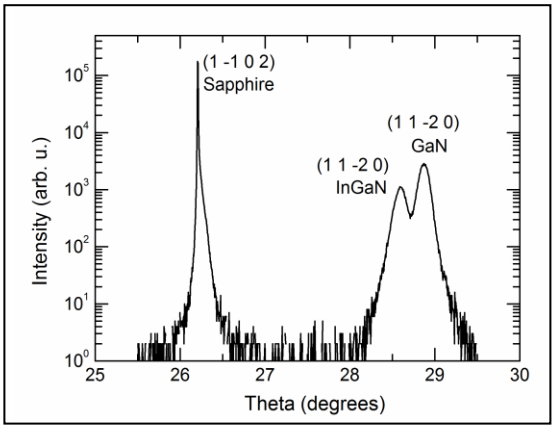

Figure 13. X-ray diffraction data showing *a*-plane $In_xGa_{1-x}N$ with x~5–9% on a GaN buffer layer atop *r*-plane sapphire.

4.1.2 THz Source

Using the ARL-grown *a*-plane InGaN films on *r*-plane sapphire, we achieved THz emission using ultrafast (~150 fs pulse width) excitation at 400 nm. The pump source, incident on the sample at 45° to the surface normal, was obtained by frequency-doubling a 250-kHz Ti:sapphire-pumped regenerative amplifier at 800 nm. The subsequent THz emission is collected with a pair of off-axis parabolic mirrors onto a zinc telluride (ZnTe) crystal for polarization sensitive EO sampling. The THz source is mounted on a 360° rotation stage for sample rotation dependence measurements. Figure 14a illustrates the orientation of the THz source relative to the incident pump beam and collected *s*- and *p*-polarized THz radiation.

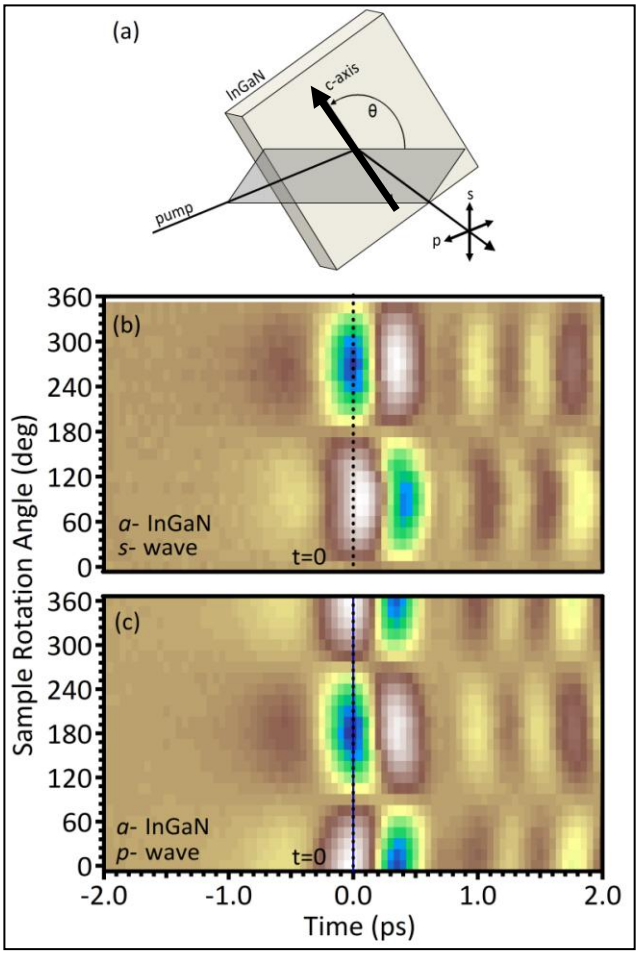

Figure 14. (a) Schematic of nonpolar InGaN rotation relative to the emitted THz polarization directions. Image plots of time-resolve (b) *s*- and (c) *p*-polarized THz waveforms from *a*-plane InGaN excited with 400 nm.

The image plots in figures 14b and c show the time-resolved *s*- and *p*-polarized THz emission from *a*-plane $In_{0.15}Ga_{0.85}N$ as a function of sample rotation, respectively. The white areas denote positive values while the blue represents negative values. Several peaks associated with water absorption may also be seen to the right of the peak THz emission. A strong dependence on the

rotation angle is observed in the image plots. To further analyze the sample rotation dependence of the *a*-plane InGaN, the THz signal at t=0 from the image plots in figure 14 is plotted in figure 15 as a function of sample rotation angle for both *s*- and *p*-polarizations. The data fit well to sinθ and cosθ functions, consistent with in-plane transport parallel to the *c*-axis direction due to SF-induced lateral electric fields. Optical rectification is neglected since it would appear as a sin(2θ) dependence.

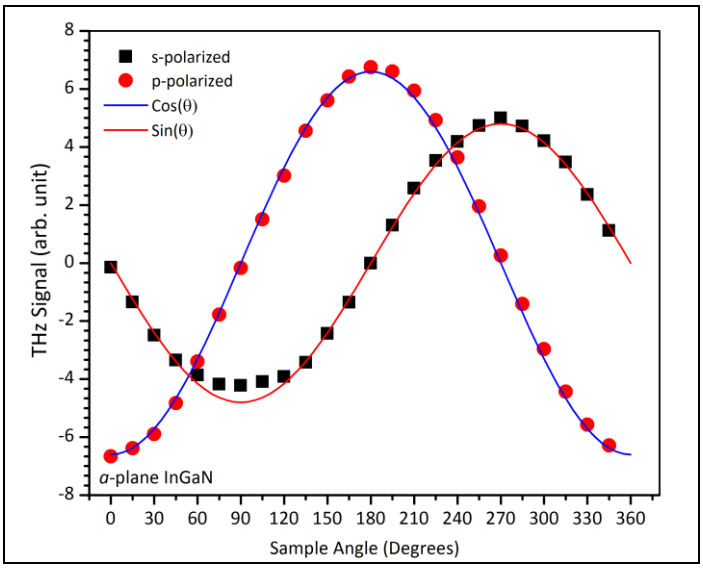

Figure 15. Sample rotation angle dependence of the peak *s*- and *p*-polarized terahertz emission (at t=0 shown in figure 6) from *a*-plane InGaN grown on *r*-plane sapphire.

For comparison, in figure 16 we plot the maximum THz emission from *a*-plane InGaN (red curve) against that from *c*-plane InGaN (black curve) under identical excitation conditions. With only initial material and SF density optimization of the *a*-plane InGaN, the THz emission from the non-polar sample is already a factor of two larger than that from the *c*-plane InGaN. THz emission from *c*-plane InGaN is attributed to the photo-Dember effect, which stems from the difference in the diffusion of photoexcited electrons and holes from the surface.

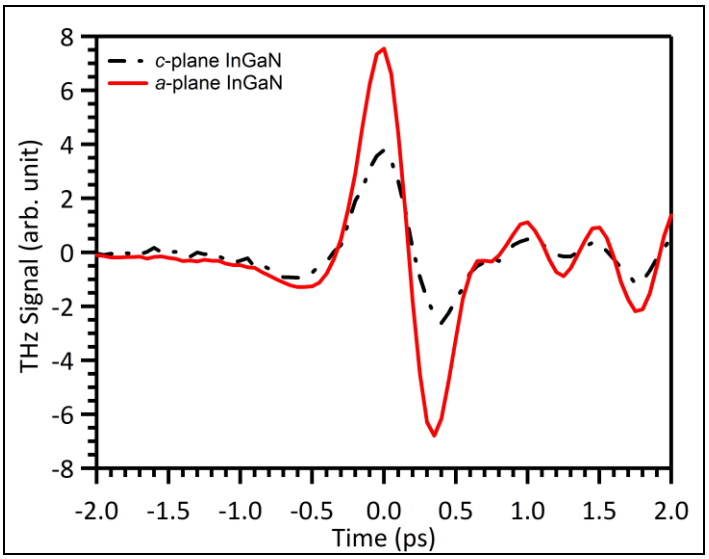

Figure 16. THz emission from *a*-plane InGaN (red curve) compared with that from *c*-plane InGaN (black curve) under identical excitation conditions.

5. High Efficiency Si Solar Cell Employing a III-nitride Active Window

InGaN solar cells can be used to extend the short wavelength performance of Si solar cells, leading to greater efficiency in energy harvesting. Si solar modules consist typically of a glass top sheet, followed by EVA encapsulation film, Si-wafer solar cells, another EVA film, and finally a back sheet of laminated fluoropolymer and other films to protect the solar panels from the environment (figure 17a). By replacing the glass top sheet with an InGaN "active window," overall efficiency can be improved by harvesting high energy photons that would otherwise be lost to heat while providing physical protection to the cell. This concept is based on a four-terminal photovoltaic (PV) heterogeneous integration of a Si and an InGaN-based PV cell, each with its own terminals (figure 17b). This approach has significant advantages that include (1) avoiding highly defective heteroepitaxy that will limit the minority carrier lifetimes and the performance of the InGaN cell, (2) improving overall device efficiency by increasing the open circuit voltage through voltage matching and (3) employing a vertical geometry that avoids the complexity of spectral splitting associated with lateral devices. In contrast to other examples investigated in this program, this device does not employ crystal growth techniques for integration but relies on wafer bonding packaging techniques.

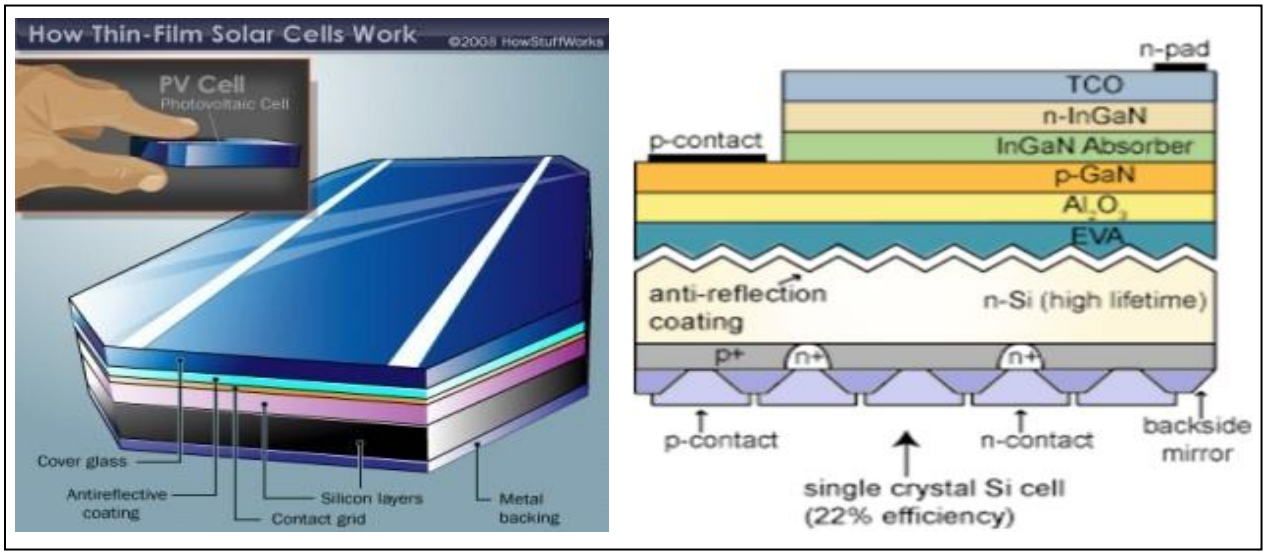

Figure 17. (a) Typical thin-film solar cell construction and (b) a schematic of an InGaN-Si EVA bonded solar cell.

Aluminum indium gallium nitride (AlInGaN) semiconductors are an ideal "active window" due to the tunability of the semiconductor's direct bandgap from 0.7 to 6.2 eV by varying the InN, GaN, and AlN mole fractions of the alloy (*17*). Furthermore, GaN has a large absorption coefficients of 10^5 cm^{-1} near the band edge (*18*), superior radiation resistance compared to other photovoltaic materials (*17*), and the potential for integration with existing Si technology (*19*). Recently, Dahal et al. (*20*) has reported InGaN solar cells with efficiencies of ~3% under concentrated sunlight. Though it is theoretically predicted that efficiencies greater than 50% are achievable with InGaN alloys with In-content of about 40% (*21*), experimental values are lower because of the difficulty in growing alloys with high InN mole fractions. In addition, the long wavelength absorption cutoff of an InGaN cell of single composition limits its efficiency. However, a broad solar spectrum absorption can be achieved by combining an InGaN solar cell with a silicon cell. During the first year of this program, we have enhanced the performance of a polysilicon solar cell by using an "active window" consisting of an InGaN solar cell on a sapphire substrate. These devices employed an InGaN cell absorbing at wavelengths shorter than 400 nm and exhibited a 15% increase in efficiency and a 30% increase in fill factor over the bare polysilicon solar cell employed.

5.1 Results

InGaN/GaN MQW solar cell structures were grown on double-side-polished 50-mm (0001) sapphire substrates by metal-organic chemical-vapor deposition (MOCVD) technique. The devices consisted of a 1-μm unintentionally doped GaN template layer, a 2-μm Si-doped n-GaN layer ([Si]=$6x10^{18}$ cm^{-3}), a 10-nm highly Si-doped n^+-GaN layer ([Si]=$2x10^{19}$ cm^{-3}), a 30-period undoped MQW active region with 2.6-nm $In_{0.2}Ga_{0.8}N$ QWs and 6.7-nm GaN barriers, a 40-nm highly Mg-doped smooth p^+-GaN layer ([Mg]=$5x10^{19}$ cm^{-3}), a 30-nm Mg-doped smooth p-GaN layer ([Mg]=$2x10^{19}$ cm^{-3}), and a 15-nm highly Mg-doped p^+-GaN contact layer. The highly Si-

doped and Mg-doped layers adjacent to the active region are necessary for screening the polarization-induced electric fields in the quantum wells (QWs), which are in the opposite direction of the p-n junction depletion field for p-side-up Ga-polar solar cells and can inhibit carrier collection if not properly accounted for in the device design (*22*). The samples were processed into solar cells using standard contact lithography processes. The final device structure consisted of 4 mm x 4 mm mesas, with 30/300 nm palladium (Pd)/gold (Au) p-contact grids on the top of each mesa with a center-to-center grid spacing of 200 μm, and 30/300 nm aluminum (Al)/Au n-contacts around the base of each mesa. A two-layer anti-reflection (AR) coating consisting of plasma-enhanced chemical vapor deposition grown silicon nitride (Si_3N_4) and SiO_2 is employed to improve absorption and performance. The device characteristics were measured by wafer-level probing at room temperature. Dark and illuminated I-V measurements were taken using Agilent HP 4156 C parametric analyzer. Broadband illumination was provided by an unfiltered Newport solar simulator with an equivalent AM1.5G illumination intensity of approximately 1.0 sun (100 mW/cm^2).

Figure 18 shows the absorption spectra of the unprocessed InGaN QW solar cell structure. The absorption was calculated from the measured transmission and reflection using a Shimadzu UV-3600 UV-visible (VIS)-near IR (NIR) spectrophotometer. This tool uses a white light source and a monochromator for the spectral measurements. The transmitted and reflected beams from the sample are collected in an integrating sphere and measured by a PMT detector. The use of an integrating sphere is of fundamental importance to thoroughly measure diffuse transmission $T(\lambda)$ and reflection $R(\lambda)$; this technique is especially useful for samples with rough or textured surfaces. The absorption of the InGaN solar structure was then determined as $A(\lambda)=1-T(\lambda)-R(\lambda)$. The absorption curve has a sharp cutoff at ~450 nm that corresponds to the absorption tail of the InGaN cell and the absorption by the sapphire substrate (*23*). The strong absorption below 365 nm is due to the GaN layer and does not contribute to photocurrent as the generated carriers have short diffusion lengths and will most likely recombine in the neutral p-GaN region. As a result, the "active window" InGaN cell in this design will harvest photons in the range between 365 to 450 nm.

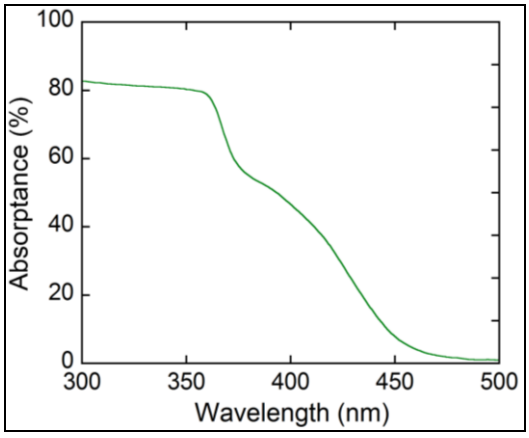

Figure 18. Absorption spectra for InGaN QW solar cell.

Experiments were performed to determine the optimal AR coating parameters for the InGaN surface so as to increase the transmission in the visible spectra range for optimal Si solar cell performance while maximizing the absorption in UV spectral region for optimal InGaN solar cell performance. The optimal AR coating for this device consisted of a 40 nm of Si_3N_4 followed by a 75 nm of SiO_2,

Commercial polysilicon solar cells were used for this study to determine the enhancement due to using InGaN as an "active glass" window. The Si solar cells were diced into four 4-mm^2 pieces and mounted onto a Si header with four metal contact pads. Figure 19 (right) shows the cross-sectional view of the hybrid structure, with four Si cells connected in series. A 16-mm^2 InGaN solar cell was used as the "active glass" to protect the four underlying Si cells and was mounted using EVA. Figure 19 (left) shows a photograph of the fabricated hybrid structure mounted onto a ceramic package with wire bonding for testing. The top n-type contacts for the Si solar cells were made using silver epoxy while the p-type metal was bonded to the extended metal pads on the fan-out to make the p-type contact. For the InGaN cell, both p- and n-contacts were made from the top of the hybrid device and wire bonded to the metal pads on the ceramic package. As shown in figure 19, the InGaN solar cell covers entirely the four Si solar cells. The two sections of the cell are integrated for voltage matching by connecting the InGaN cell in parallel with the four Si cells connected in series.

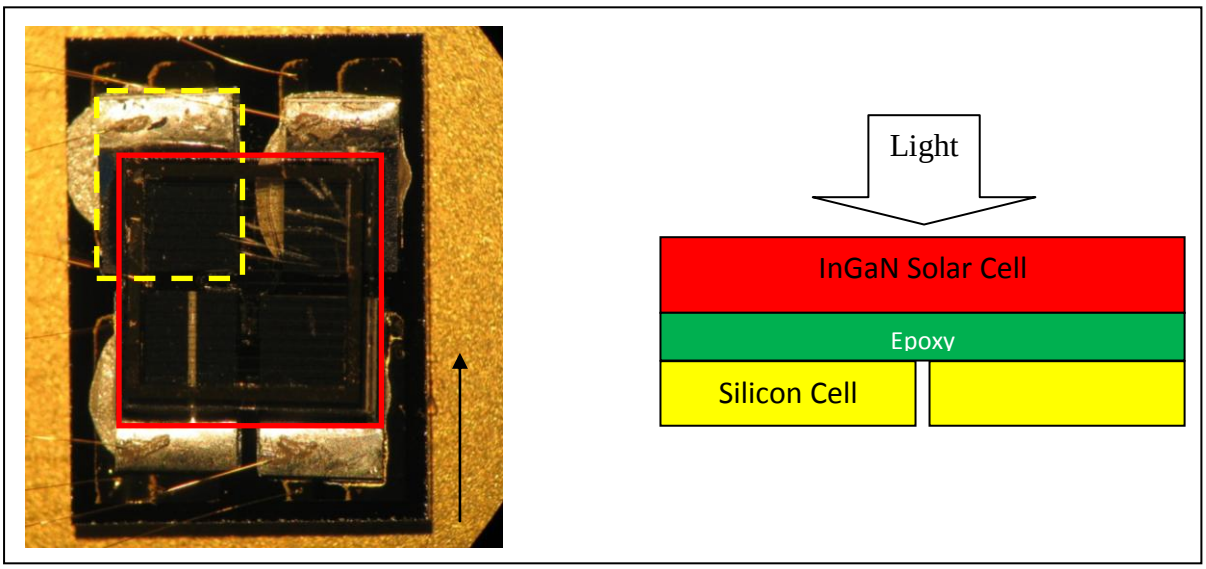

Figure 19. (Left) Photo of InGaN-Si active window solar cell and (right) cross-sectional view of solar cell with the InGaN window outlined in red, and a Si cell outlined in broken yellow.

The I-V characteristics of InGaN solar cells under illumination and with and without AR coating are shown in figure 20. While both devices exhibit an open circuit voltage (V_{oc}) of 2.0 V independent of coating, the short circuit current (I_{sc}) is about 20% higher for the device with the

AR coating compared to the device without due to the increase absorption in the structure. The observed photovoltaic response for these devices is comparable to the results from similar devices reported by Farrell et al. (*19*).

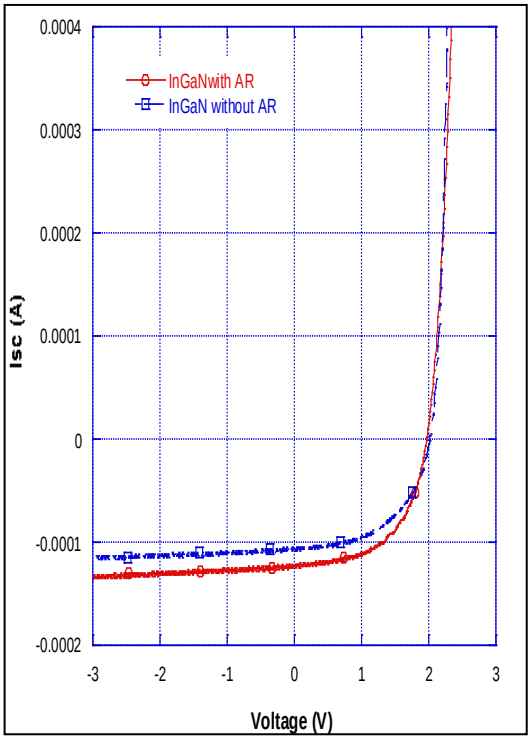

Figure 20. I-V curves for InGaN solar cell with and without AR coating.

Figure 21 shows the I-V curves of a single Si solar cell and the hybrid solar cell with the InGaN "active glass" window. The four Si solar cells when connected in series produce a V_{oc} of about 2.0 V. By using the obtained data from experimental I-V curves, the calculated efficiency (η) and fill factor of the Si solar cells are calculated to be 7.6% and 42%, respectively. This low value of Si solar cell efficiency is representative of the as received polysilicon solar cell efficiency prior to dicing. Future efforts will include Si cells with higher starting efficiencies. By comparing the I-V curves of the four Si cells with and without InGaN solar cell, we observed that the V_{oc} is same 2.0 V for both the configurations. However, we observed about 10% increases in short circuit current for the hybrid structure in which InGaN solar cell is in operation. The efficiency (η) and fill factor of the hybrid structure calculated from experimental I-V curves are 8.7 % and 54%, respectively. Hence, by comparing the efficiency and fill factor for the hybrid structure with the Si solar cells, we obtained not only an increase of about 15% in efficiency but also about 30% increase in fill factor. This increase in overall collection efficiency is attributed to additional photo carriers generated in the InGaN solar cell in the UV spectral range, which was not collected by the Si solar cell. By optimizing the InGaN design and fabrication process one can achieve higher efficiency solar cell, which will improve the performance of hybrid solar cell structure. Though a reliability study has not been performed, the

hybrid structure should have a longer lifetime, as the UV light is now being absorbed by the InGaN solar cell "active glass" as opposed to the Si solar cells, which typically leads to heat generation resulting in lower performance.

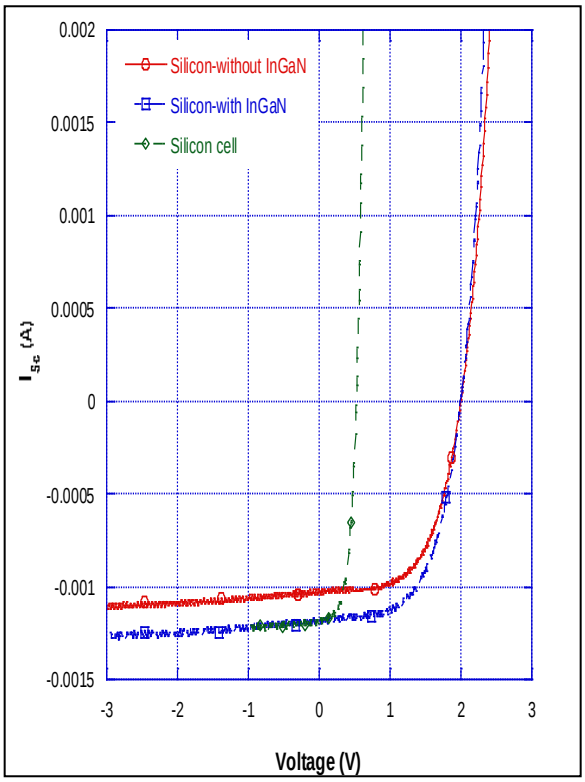

Figure 21. I-V curves for Si cell only, hybrid cell with and without InGaN cell in operation.

6. Conclusion

Heterogeneous architectures incorporating III-Nitride semiconductor with other materials hold great promise for realizing optoelectronic devices with improved performance that are not currently possible with either material on its own. These devices include solar blind separate absorption and multiplication APDs, near-UV LDs, compact terahertz sources and emitters, as well as high efficiency solar cells that have direct application for Army systems for biological agent identification and detection, scintillation-based radiation detection, standoff explosive detection, and compact renewable power sources. During the fiscal year 2011 program, we have demonstrated heterogeneous III-Nitride/SiC SAM-APDs that exhibit the high gain (>1000) and low dark currents (<0.1 nA near avalanche breakdown) generally associated with SiC-based APDs, while improving the near-UV response by a factor of ~three by incorporating a GaN absorption region. In addition, we have demonstrated a THz emitter based on heterogeneous

InGaN that is excitable using a 400-nm laser source. The efficiency of a commercial Si solar cell was improved through the incorporation of a GaN active window that harvests high energy photons generally lost to heat within the Si cell. Finally, the initial process steps for fabrication a III-Nitride/ MgZnO-based LD were demonstrated, including the growth of p-type GaN on ZnO epilayers deposited on a bulk ZnO substrate. For most of these examples, we observe that the heterointerface plays a critical role in device performance and must be further understood to improve device performance.

7. References

1. Danielsson, E.; Zetterling, C.-M.; Ostling, M.; Linthicum, K.; Thomson, D. B.; Nam, O.-H.; Davis, R. F. The Influence of Band Offsets on the IV Characteristics for GaN/SiC Heterojunctions. *Sol. State Electron* **2002**, *46*, 827–35.

2. Limb et al, *APL* **2006**, *89*, 011112.

3. Ng, B. K.; David, J.P.R.; Tozer, R. C.; Rees, G. J.; Yan, F.; Zhao, J. H.; Weiner, M. *IEEE T Electron Dev* **2003**, *50* (8), 1724–1732.

4. Özgür,Ü.; Alivov, Ya. I.; Liu, C.; Teke, A.; Reshchikov, M. A.; Doğan, S.; Avrutin, V.; Cho, S.-J.; Morkoc, H. A Comprehensive Review of ZnO Materials and Devices. *J. of Appl. Phys.* **2005**, *98*, 041301. *And references therein.*

5. Yoshida, H.; Yamashita, Y.; Kuwabara, M.; Kan, H. A 342-nm Ultraviolet AlGaN Multiple-quantum-well Laser Diode. *Nature Photonics* **2008**, *2*, 551.

6. Wagner, M. R.; Callsen, G.; Reparaz, J. S.; Schultz, J.-H.; Kirste, R.; Cobet, M.; Ostapenko, I. A.; Rodt, S.; Nenstiel, C.; Kaiser, M.; Hoffmann, A.; Rodina, A. V.; Phillips, M. R.; Lautenschlager, S.; Eisermann, S.; Meyer, B. K. Bound Excitons in ZnO: Structural Defect Complexes versus Shallow Impurity Centers. *Phys. Rev. B* **2011**, *84*, 035313.

7. Simon, John; Protasenko, Vladimir; Lian, Chuanxin; Xing, Huili; Jena, Debdeep. Polarization-Induced Hole Doping in Wide-Band-Gap Uniaxial Semiconductor Heterostructures. *Science* **2010**, *327*, 60.

8. Veal, T. D.; King, P.D.C.; Hatfield, S. A.; Bailey, L. R.; McConville, C. F.; Martel, B.; Moreno, J. C.; Fryssinet, E.; Semond, F.; Zúñiga-Pérez, J. Valence Band Offset of the ZnO/AlN Heterojunction Determined by Xray Photoemission Spectroscopy. *Appl. Phys. Lett.* **2008**, *93*, 202108.

9. Metcalfe, G. D.; Shen, H.; Wraback, M.; Hirai, A.; Wu, F.; Speck, J. S. *Appl. Phys. Lett.* **2008**, *92*, 241106.

10. Metcalfe, G. D.; Shen, H.; Wraback, M.; Koblmüller, G.; Gallinat, C.; Wu, F.; Speck, J. S. *Appl. Phys. Express* **2010**, *3*, 092201.

11. Metcalfe, G. D.; Shen, H.; Wraback, M.; Hiari, A.; Koblmuller, G.; Gallinat, C.; Speck, J. *physica status solidi c* **2010**, *7* (10), 2455–2458.

12. Chern, G. D.; Readinger, E. D.; Shen, H.; Wraback, M.; Gallinat, C. S.; Koblmuller, G.; Speck, J. S. *Appl. Phys. Lett*. **2006**, *89*, 141115.

13. Miller, D. A.; Chemla, D. S.; Damen, T. C.; Gossard, A. C.; Wiegmann, W.; Wood, T. H.; Burrus, C. A. *Phys. Rev. B* **1985**, *32*, 1043.

14. Sha, W.; Norris, T. B.; Burm, J. W.; Woodard, D.; Schaff, W. J. *Appl. Phys. Lett.* **1992**, *61*, 1763.

15. Wraback, M.; Shen, H.; Dutrta, M. US Patent #6476596, 11/05/2002.

16. Misra, P.; Sun, Y. J.; Brandt, O.; Grahn, H. T. *J. Appl. Phys.* **2004**, *96*, 7029.

17. Wu, J. Q. *J. Appl. Phys.* **2009**, *106*, 011101.

18. David, A.; Grundmann, M. J. *Appl. Phys. Lett.* **2010**, *97*, 033501.

19. Reichertz, L. A.; Gherasoiu, I.; Yu, K. M.; Kao, V. M.; Walukiewicz, W.; Ager, J. W. *Appl. Phys. Express* **2009**, *2*, 122202.

20. Dahal, R.; Li, J.; Aryal, K.; Lin, J. Y.; Jiang, H. X. InGaN/GaN Multiple Quantum Well Concentrator Solar Cells. *Applied Physics Letters* **2010**, *97*, 073115.

21. De Vos, A. *Endoreversible Thermodynamics of Solar Energy Conversion;* Oxford University Press, Oxford, p. 90 (1992).

22. Wierer, J. J.; Fischer, A. J.; Koleske, D. D. *Appl. Phys. Lett.* **2010**, *96*, 051107.

23. Matioli, E.; Neufeld, C.; Iza, M.; Cruz, S. C.; Al-Heji, A. A.; Chen, X.; Farrell, R. M.; Keller, S.; Debars, S.; Mishra, U.; Nakamura, S.; Speck, J.; Weisbuch, C. *Applied Physics Letters* **2011**, *98*, 021102.

24. Farrell, R. M.; Neufeld, C. J.; Cruz, S. C.; Lang, J. R.; Iza, M.; Keller, S.; Nakamura, S.; DenBaars, S. P.; Mishra, U. K.; Speck, J. S. *Applied Physics Letters* **2011**, *98*, 201107.

8. Transitions

This work has generated the following papers and presentations:

1. Wraback, M.; Sampath, A. V.; Enck, R. W.; Shen, H.; Zhou, Q.; McIntosh, D.; Campbell, J. Hybrid III-nitride/SiC Ultraviolet Avalanche Photodiodes. invited presentation at the *Workshop on Compound Semiconductor Materials and Devices*, Savannah, GA, February 2011.

2. Shen, H.; Sampath, A. V.; Zhou, Q.; Campbell, J.; Wraback, M. Effect of Interface Polarization Charge on GaN/SiC Separate Absorption and Multiplication Avalanche Photodiodes. invited presentation at *2011 Electrochemical Society Meeting*, Boston, MA.

3. Sampath, A. V; Enck, R. W.; Shen, H.; Zhou, Q.; McIntosh, D.; Campbell, J.; Wraback, M. III-nitride/SiC Separate Absorption and Multiplication Avalanche Photodiodes. invited presentation at *West Virginia University Graduate Student Seminar*, Morgantown, WV, October 2011.

4. Sampath, A. V.; Enck, R. W.; Shen, H.; Zhou, Q.; McIntosh, D.; Campbell, J.; Wraback, M. Impact of Hetero-interface on the Photoresponse of GaN/SiC Separate Absorption and Multiplication Avalanche Photodiodes. invited presentation at *2011 International Semiconductor Device Research Symposium*, College Park, MD, December 2011.

5. Sampath, A. V.; Enck, R. W.; Shen, H.; Wraback, M.; Zhou, Q.; McIntosh, D.; Campbell, J. III-nitride/SiC Separate Absorption and Multiplication Avalanche Photodiodes: The Importance of Controlling Polarization-Induced Interface Charge. *Int. J. of High Speed Electron. and Systems* **2011**, *20*, 487.

6. Zhou, Q.; McIntosh, D.; Lu, Z.; Campbell, J.; Sampath, A. V.; Shen, H.; Wraback, M. GaN/SiC Avalanche Photodiodes. *Appl. Phys. Lett.* **2011**, *99*, 131110.

7. Wraback, M.; Shen, H.; Sampath, A. V. Polarization Enhanced Avalanche Photodetector and Method Thereof, filed in U.S. Patent and Trademark Office, May, 2011.

8. Shen, H.; Wraback, M.; Sampath, A. V. Semiconductor Photodetector with Transparent Interface Charge Control Layer and Method Thereof, filed in U.S. Patent and Trademark Office, May 2011.

9. Metcalfe, G. D.; Gallinat, C. S.; Shen, H.; Wraback, M.; Wienecke, S.; Young, E. C.; Speck, J. S. Effects of Strain Relaxation on the Photoluminescence of Semipolar InGaN. submitted to *Conference on Lasers and Electro-Optics*, 2012.

10. Woodward, N. T.; Metcalfe, G. D.; Enck, R.; Gallinat, C. S.; Shen, H.; Wraback, M. THz Emission from a-plane InGaN. submitted to *Conference on Lasers and Electro-Optics*, 2012

11. Garrett, G. p-GaN/MgZno Optoelectronic Devices Grown on Bulk ZnO. to be presented at the *48th Annual Workshop on Compound Semiconductor Materials and Devices*, WOCSEMMAD 2012, February 19–22, Napa, CA.

The work on bulk ZnO is being leveraged for the FY12-SED-50 Coherent Optical Control Director's Research Initiative (DRI).

List of Symbols, Abbreviations, and Acronyms

AFM	atomic force microscopy
Al	aluminum
AlGaN	aluminum gallium nitride
AlInGaN	aluminum indium gallium nitride
AlN	aluminum nitride
APDs	avalanche photodiodes
AR	anti-reflection
Ar	argon
ARL	U.S. Army Research Laboratory
Au	gold
CBM	conduction band offset
CCD	charge-coupled device
Cl_2	chlorine
ECBC	Edgewood Chemical and Biological Center
EO	electro-optic
FOBs	forward operating bases
FY11	fiscal year 2011
Ga	gallium
GaN	gallium nitride
In	indium
InGaAs	indium gallium arsenide
InN	indium nitride
InP	indium phosphide
IR	infrared

I-V	current voltage
LDs	laser diodes
LEDs	light-emitting diodes
LIDAR	light detection and ranging
MBE	molecular beam epitaxy
Mg	magnesium
MgO	magnesium oxide
MgZnO	magnesium zinc oxide
MOCVD	Metal-organic chemical-vapor deposition
MQW	multi quantum well
Nd	neodymium
Ni	nickel
NIR	near IR
PAMBE	plasma assisted molecular beam epitaxy
PC	photoconductive
Pd	palladium
PICCL	p-type interface charge control layer
PL	photoluminescence
PMTs	photomultiplier tubes
PV	photovoltaic
QE	quantum efficiency
QW	quantum well
RGA	residual gas analysis
RHEED	reflection high energy electron diffraction
RMS	root mean square
SAM	separate absorption and multiplication
SEM	scanning electron microscopy

SF	stacking-fault
Si	silicon
SiC	silicon carbide
Si_3N_4	silicon nitride
SiO_2	silicon dioxide
TAC-BIO	tactical-biological
THz	terahertz
Ti	titanium
TEM	transmission electron microscopy
UCF	University of Central Florida
UID	unintentional doping
UV	ultraviolet
VBM	valence band maximum
VIS	visible
Xe	xenon
YAG	yttrium aluminum garnet
Zn	zinc
ZnO	zinc oxide
ZnTe	zinc telluride
$ZnTiO_3$	zinc titanate

NO. OF COPIES	ORGANIZATION
1 ELEC	ADMNSTR DEFNS TECHL INFO CTR ATTN DTIC OCP 8725 JOHN J KINGMAN RD STE 0944 FT BELVOIR VA 22060-6218
7	US ARMY RSRCH LAB ATTN IMNE ALC HRR MAIL & RECORDS MGMT ATTN RDRL CIO LL TECHL LIB ATTN RDRL CIO LT TECHL PUB ATTN RDRL SEE M ANAND V SAMPATH MEREDITH L REED MICHAEL GERHOLD MICHAEL WRABACK ADELPHI MD 20783-1197
TOTAL:	8 (7 HCS, 1 ELEC)